50th AIAA Aerospace Sciences Meeting including the New Horizons Forum and Aerospace Exposition
09 - 12 January 2012, Nashville, Tennessee

AIAA 2012-0428

Wake Evolution of Wing-Body Configuration from Roll-Up to Vortex Decay

Takashi Misaka[*], Frank Holzäpfel[†] and Thomas Gerz[†]

Deutsches Zentrum für Luft- und Raumfahrt (DLR), 82234 Oberpfaffenhofen, Germany

The development of aircraft's wake vortex from the roll-up until vortex decay is studied. An aircraft model and the surrounding flow field obtained from high-fidelity Reynolds-averaged Navier-Stokes simulation are swept through a ground-fixed computational domain to initialize the wake. After the wake initialization, the large-eddy simulation of the vortical wake is performed until vortex decay. The methodology is tested with the NACA0012 wing and applied to the DLR-F6 wing-body model. The roll-up process of the vorticity sheet from a main wing and the merge of an inboard wing vortex into the wingtip vortex are simulated. Vortex parameters such as the radially averaged circulation, vortex core radius and vortex separation are also evaluated. The growth rate of the vortex core radius is relatively small during the roll-up where the fine mesh resolution in the LES is required to capture the tiny vortex core in the RANS simulation.

I. Introduction

Wake vortices generated by a flying aircraft pose a potential risk for following aircraft due to the strong and coherent vortical flow structure.[1] In addition, it is pointed out that condensation trails (contrails) originated from the interaction of jet exhaust, wake vortices and the environmental atmosphere may trigger the formation of cirrus clouds (contrail cirrus) which have influence on the climate.[2,3] Wake vortex is related to a broad scale of flows. Flows around aircraft's main wing, fuselage, slat, flap, jet engine and tail plane, and their interactions may affect the generation of wake vortex in particular in a high-lift condition.[4] On the other hand, contrails generated by cruising aircraft spread several tens kilometers.

The evolution of aircraft's wake can be divided into several phases, for example, (1) roll-up phase, (2) vortex phase, and (3) dissipation phase. Although numerical simulation is one of the effective approaches to tackle this problem, the applicable flow scale of a numerical simulation code is usually limited to each of those regimes. High-fidelity Reynolds-averaged Navier-Stokes (RANS) simulations can handle flows around aircraft and subsequent roll-up process of wake vortex in the jet regime.[5] In addition, experimental measurements of near field wake evolutions have been conducted.[4,6] On the other hand, the dynamics of rolled-up wake vortex in the vortex and dissipation regime has been studied mainly by Large-eddy simulation (LES) or direct numerical simulation (DNS). In these researches, detailed time evolution of a vortex pair with a longitudinally constant velocity profile is investigated, where short-wave (elliptic) instability[7–9] and Crow instability[10,11] may develop. In addition, various atmospheric conditions of turbulence, stability and wind shear are considered to assess the effect of these factors on wake vortex evolution and decay.[12–14] The LES of wake vortex in the late dissipation and diffusion regimes is performed along with microphysical processes of contrails where microphysical processes of contrails are of primary interest.[15,16]

The authors investigated the feasibility of a wake initialization approach where realistic aircraft wake is generated in a LES domain by sweeping a high-fidelity RANS flow field through the domain.[17] Using this approach the simulation was performed from the roll-up of the DLR-F6 wing-body model until the vortex decay. The preliminary results revealed several points to be overcome to use the this approach: the connection of turbulent quantity such as eddy viscosity not only the connection of a velocity field, a sophisticated way to define the switching wall-distance between RANS and LES flow fields instead of using a constant wall-distance.

---

[*]Research Assistant, Institut für Physik der Atmosphäre, Münchner Straße 20, Member AIAA.
[†]Research Scientist, Institut für Physik der Atmosphäre, Münchner Straße 20, Member AIAA.

This paper focuses on the above mentioned points of the present approach and investigates the evolution of vortex parameters such as the radially averaged circulation, vortex core radius and vortex separation from the wake roll-up to vortex decay. Here we consider a simple NACA0012 wing for the numerical tests of the approach. Then the DLR-F6 model in a cruise condition is investigated with and without employing an ambient turbulence field. The study bridging the gap between the roll-up and the vortex phases shall provide more realistic insights into aircraft wake vortex evolution expressed in terms of e.g., vortex circulation and vortex core radius. It also allows investigating the entrainment of jet exhaust by considering tracers, which might be useful for detailed contrail modeling studies.

II.   Governing equations and numerical methods

The LES is performed by using incompressible Navier-Stokes code MGLET.[18] An equation for potential temperature is also solved to take into account buoyancy effects of the atmosphere.

$$\frac{\partial u_i}{\partial t} + \frac{\partial (u_i u_j)}{\partial x_j} = -\frac{1}{\rho_0}\frac{\partial p'}{\partial x_i} + (\nu + \nu_t)\frac{\partial^2 u_i}{\partial x_j^2} + g\frac{\theta'}{\theta_0}\delta_{i3}\,, \tag{1}$$

$$\frac{\partial \theta'}{\partial t} + \frac{\partial (u_j \theta')}{\partial x_j} = (\kappa + \kappa_t)\frac{\partial^2 \theta'}{\partial x_j^2} + u_3\frac{d\theta_s}{dx_3}\,, \tag{2}$$

$$\frac{\partial u_j}{\partial x_j} = 0\,, \tag{3}$$

where u_i, p' and θ' represent velocity components in three spatial directions (i=1, 2 or 3), pressure and potential temperature, respectively. Summation convention is used for velocity components u_i and δ_{ij} denotes Kronecker's delta. The primes for pressure and potential temperature show that these are defined by the deviation from the reference states: $p = p_0 + p'$, $\theta = \theta_0 + \theta'$. In the Boussinesq approximation, the potential temperature is coupled to momentum equations through the vertical velocity component. Kinematic viscosity in Eq. (1) is given by the sum of molecular viscosity and eddy viscosity defined by a subgrid-scale model. Corresponding diffusion coefficient κ in Eq. (2) is obtained by assuming constant molecular and turbulent Prandtl numbers of 0.7 and 0.9, respectively.

The above equations are solved by a finite-volume approach with the fourth-order finite-volume compact scheme.[19, 20] A split-interface algorithm is used for the parallelization of the tri-diagonal system, which realize smaller overhead time and scalability in parallel environment compared to the existing parallel tri-diagonal matrix solvers.[21] In addition, a divergence free interpolation is employed for obtaining advection velocity, which ensures conservation of velocity and passive tracer fields. A pressure field is obtained by the velocity-pressure iteration method[22] with a multi-grid convergence acceleration technique.[23] The third-order Runge-Kutta method is used for the time integration.[24] The Lagrangian dynamic model is employed for a turbulence closure.[25] The Lagrangian dynamic model does not require specific direction for the averaging process of subgrid model coefficients which is usually required in dynamic-type models for stable computation, therefore, the Lagrangian dynamic model is appropriate for wake vortex simulation where there is no relevant direction for the averaging. Computations are performed in parallel by a domain decomposition approach.

III.   Description of present approach

The present approach which is schematically shown in Fig. 1 could be a numerical realization of the catapult wind tunnel.[26] The numerical approach has several advantages for investigating aircraft wake. Decay of a vortex pair strongly depends on environmental conditions such as ambient turbulence, temperature stratification and wind shear. Therefore the control of these conditions is crucially important to assess the influence of the ambient conditions on vortex decay. Unlike the consideration of realistic inflow conditions in an aircraft fixed LES domain, the generation of controlled turbulence fields in the ground fixed LES domain is straightforward. The other reason is that the present approach does not need a long computational domain in the flight direction for obtaining longer vortex age compared to an aircraft fixed LES domain.

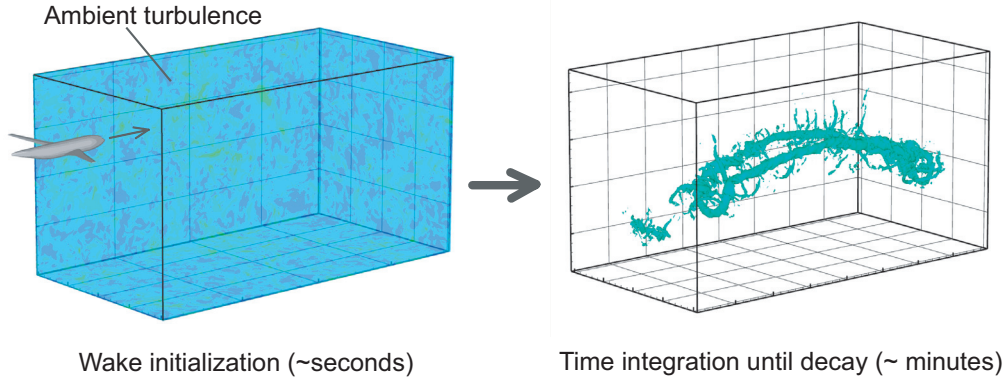American Institute of Aeronautics and Astronautics

Figure 1. Schematic of the present approach, (a) wake initialization in the order of seconds, (b) wake evolution in the order of several minutes until vortex decay.

III.A.   Wake initialization using RANS flow field

An aircraft model and the surrounding flow field obtained from high-fidelity RANS simulation are swept through a ground fixed LES domain to initialize the aircraft's wake.[17] The RANS flow field is provided as a forcing term of Navier-Stokes equations in the LES. Similar approach might be referred to as the fortified solution algorithm (FSA),[27] or a nudging technique used in data assimilation.[28] The resulting velocity field is represented by the weighting sum of LES velocity field $\boldsymbol{V}_{\mathrm{LES}}$ and RANS velocity field $\boldsymbol{V}_{\mathrm{RANS}}$,

$$\boldsymbol{V} = f(y,\alpha,\beta)\boldsymbol{V}_{\mathrm{LES}} + [1 - f(y,\alpha,\beta)]\,\boldsymbol{V}_{\mathrm{RANS}}\,. \tag{4}$$

In this study, $\boldsymbol{V}_{\mathrm{RANS}}$ is provided as a constant forcing term of Navier-Stokes equations solved in the LES as a one-way coupling. Since the aircraft model is swept through a computational domain, the forcing term acts as a moving boundary condition for the LES. The weighting function $f(y,\alpha,\beta)$ could be a smooth function of the wall-distance y, or of other physical quantities such as velocity magnitude. Here, we employ the following function of wall-distance to realize smooth transition between the RANS and LES flow fields,

$$f(y,\alpha,\beta) = \frac{1}{2}\left[\tanh\left[\alpha\left(\frac{y}{\beta} - \frac{\beta}{y}\right)\right] + 1.0\right], \tag{5}$$

where the constants α and β represent the slope of the transition and the wall-distance where solutions of RANS and LES are equally weighted, respectively. These constants can be determined by try and error, as well as by optimization techniques.

The mapping of the RANS flow field onto the Cartesian LES mesh is performed by a linear interpolation only once before the wake initialization. An additional computer memory is prepared to store the mapped RANS flow field, however, the additional computational cost for the forcing term is minimal. The forward movement of an aircraft is represented by simply shifting the mapped flow field for a certain mesh spacing, which is also possible for a decomposed LES domain if the increments of the advancement is smaller than the halo region of the domain decomposition for parallel computation.
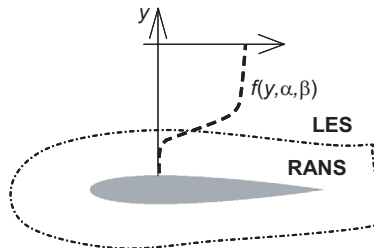

Figure 2. Schematic of a weighting function for a combination of RANS and LES flow fields.

American Institute of Aeronautics and Astronautics

III.B.   Reproduction of eddy viscosity

Since we only use a RANS velocity field to initialize the wake, the eddy viscosity in the LES domain appears to be low compared to that in the original RANS flow field. Therefore it is required to reproduce velocity fluctuations modeled in the RANS flow field. It is pointed out that the correct representation of eddy viscosity in the wake is important to simulate the wake evolution.[29]

Most crude but still useful representation of such velocity fluctuations may be a white noise. Here we add a white noise to the RANS flow field in the region of RANS-LES transition so that the time averaged LES eddy viscosity matches to the RANS eddy viscosity in the wake. The magnitude of the fluctuations is modified by the proportional-integral (PI) controller during the advancement of the model through the LES domain.

$$\boldsymbol{V}_{\mathrm{RANS+WN}} = \boldsymbol{V}_{\mathrm{RANS}} + K\boldsymbol{V}_{\mathrm{WN}}, \tag{6}$$

$$K = a_1 \left(\bar{\mu}_{t,\mathrm{LES}} - \mu_{t,\mathrm{RANS}} \right) + a_2 \int \left(\bar{\mu}_{t,\mathrm{LES}} - \mu_{t,\mathrm{RANS}} \right) dt, \tag{7}$$

where $\boldsymbol{V}_{\mathrm{WN}}$ is a white noise field and K is a gain to control the magnitude of the velocity fluctuations. The gain is defined by the difference between the time-averaged LES eddy viscosity $\bar{\mu}_{t,\mathrm{LES}}$ and RANS eddy viscosity $\mu_{t,\mathrm{RANS}}$. These eddy viscosities for calculating the gain are integrated in the wake region with the weighting of the RANS eddy viscosity. The magnitude of the added white noise is also weighted locally using the RANS eddy viscosity. The constants a_1 and a_2 are set according to the convergence of the gain and numerical stability but the results are not too sensitive to these values.

III.C.   Optimization of RANS-LES interface

In the above formulation, RANS and LES flow fields are switched using a certain threshold, i.e., a constant distance from the body surface. On the other hand, it is also possible to define the wall-distance locally by using optimization techniques with respect to an appropriate cost function. We tested a cost function defined by the difference of axial vorticity magnitudes at two different locations in flight direction,

$$J(\alpha, \beta) = \frac{1}{2} \left[\omega_{x2} - \omega_{x1} \right]^2, \tag{8}$$

$$\omega_x = (\nabla \times \boldsymbol{V})_x, \quad \omega_{x1} = (\nabla \times \boldsymbol{V})_x |_{x=x_1}, \quad \omega_{x2} = (\nabla \times \boldsymbol{V})_x |_{x=x_2}. \tag{9}$$

This cost function is evaluated locally, i.e., the upstream axial vorticity magnitude ω_{x2} at x_2 and the downstream axial vorticity ω_{x1} at x_1 are evaluated at each grid point within the RANS-LES transition region. The cost function is minimized by gradient-based optimization methods. The gradients of the cost function are obtained as follows,

$$\nabla_\alpha J(\alpha, \beta) = \left(\frac{\partial f}{\partial \alpha} \right)^T \left[\delta\omega_{x2} - \delta\omega_{x1} \right] \left[\omega_{x2} - \omega_{x1} \right], \tag{10}$$

$$\nabla_\beta J(\alpha, \beta) = \left(\frac{\partial f}{\partial \beta} \right)^T \left[\delta\omega_{x2} - \delta\omega_{x1} \right] \left[\omega_{x2} - \omega_{x1} \right], \tag{11}$$

$$\delta\omega_x = \left[\nabla \times (\boldsymbol{V}_{\mathrm{LES}} - \boldsymbol{V}_{\mathrm{RANS}}) \right]_x, \tag{12}$$

$$\delta\omega_{x1} = \left[\nabla \times (\boldsymbol{V}_{\mathrm{LES}} - \boldsymbol{V}_{\mathrm{RANS}}) \right]_x |_{x=x_1}, \tag{13}$$

$$\delta\omega_{x2} = \left[\nabla \times (\boldsymbol{V}_{\mathrm{LES}} - \boldsymbol{V}_{\mathrm{RANS}}) \right]_x |_{x=x_2}. \tag{14}$$

Here the derivation of the switching function f with respect to parameters α and β can be obtained analytically from Eq. (5). Using this gradient, the search direction is defined based on the conjugate gradient method. In addition, the average of parameters α and β in the wall-normal direction is required to realize a sufficiently smooth distribution of the switching function.

The numerical cost for the optimization is not large because the additional computations of the cost function Eq. (8) and the gradients are only needed. However, the average of the parameters α and β requires a wide stencil in the order of the switching distance which can be larger than the halo region for the domain-decomposed parallel computation. In that case, the extra information exchange between decomposed domains is needed.

American Institute of Aeronautics and Astronautics

IV. Numerical test using the NACA0012 wing

Numerical tests of the present approach are performed by using a simple rectangular wing. The wing has a NACA0012 cross-section and a rounded wing-tip. An inflow velocity of 52 m/s and an angle of attack of 10 degrees are considered. A wind tunnel test of this configuration was conducted by Chow *et al.*[30] and numerical studies followed that configuration to investigate higher-order schemes, turbulence models and so on.[31] Figure 3 shows a computational domain for RANS simulation to obtain the near flow field and a longer domain for sweeping the RANS flow field based on the present approach. In Fig. 3, the axial velocity and the computational mesh are shown in the RANS domain. In addition, pressure on the root-side wall and iso-surface of vorticity magnitude are shown in the LES domain. For the RANS simulation, an incompressible flow solver from a free CFD software package, OpenFOAM, is used.[32]
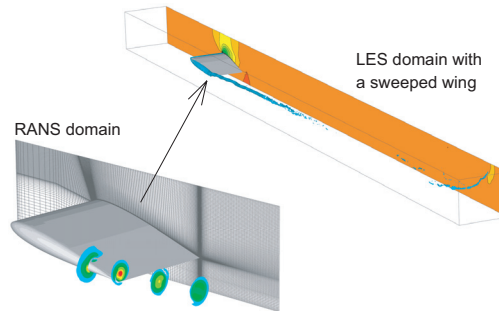
Figure 3. Computational domains for RANS simulation and LES.

Experimental[30] and RANS results as well as the results from the present approach are compared in Figures 4 and 5. Figure 4 shows the pressure coefficient along the vortex centerline where the origin of x^* is set to the trailing edge of the wing and it is normalized by the wing chord length. In addition to experimental and the RANS result, two sets of parameters ($\alpha = 1.2$, $\beta = 0.06$), ($\alpha = 1.6$, $\beta = 0.13$) for two different mesh resolutions ($dx^* = 0.005$, 0.01) are considered in the present approach. As in Fig. 4, pressure in the vortex center increases quickly in the RANS case which indicates an early decay or diffusion of the vortex in the present RANS simulation. It is mainly due to less number of mesh points and low order numerical scheme compared to other RANS simulations.[31] On the other hand, the present approach uses only the near field of the RANS flow field, therefore, it shows better results compared to the present RANS case. The case with a parameter set ($\alpha = 1.2$, $\beta = 0.06$) and fine mesh appears close to the experiment. In the coarse mesh cases, there are kinks of the pressure coefficient near the switching wall-distances of $\beta = 0.06$ and 0.13. Figure 5 shows the axial velocity along the vortex centerline. All the cases from the present approach appear to be low compared to the experiment. Unlike the pressure coefficient, there is no kink near the switching wall-distance in the coarse mesh cases. It is also confirmed that the axial velocity in the present RANS simulation decreases quickly.
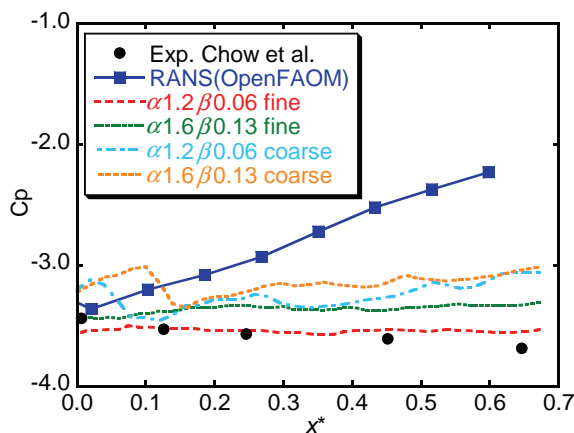

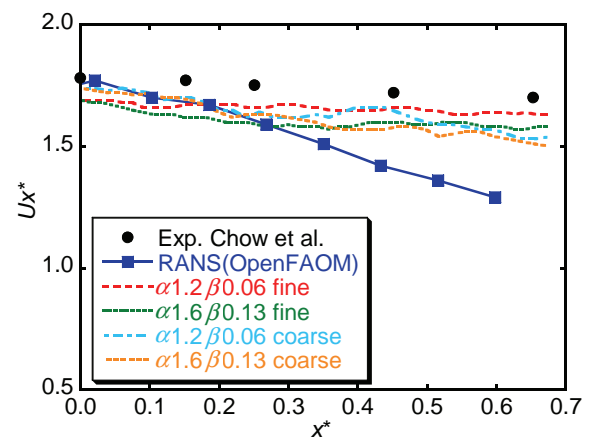**Figure 4. Pressure coefficient along the vortex centerline.**

Figure 5. Axial velocity along the vortex centerline.

Figure 6 shows the switching wall-distance of RANS and LES flow fields by green transparent surfaces before the optimization in Fig. 6(a) and after the optimization in Fig. 6(b). Vorticity iso-surface in red shows the wing-tip vortex. The switching wall-distance is decreased near the wingtip vortex in Fig. 6(b). Figure 7 shows the result with the optimization of the switching wall-distance based on the cost function in Eq. (8). The kink of the pressure coefficient in the coarse mesh case is alleviated by modifying the switching wall-distance locally.

(a)   (b)
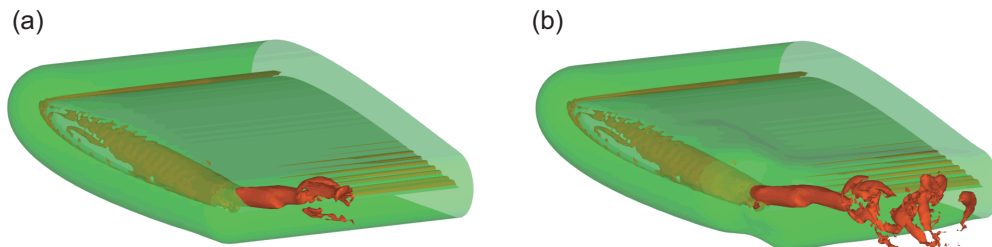
Figure 6. Iso-surface of the switching wall-distance β (green transparent) and vorticity magnitude (red) for (a) constant $\beta = 0.13$ and (b) locally optimized β based on the cost function Eq. (8).
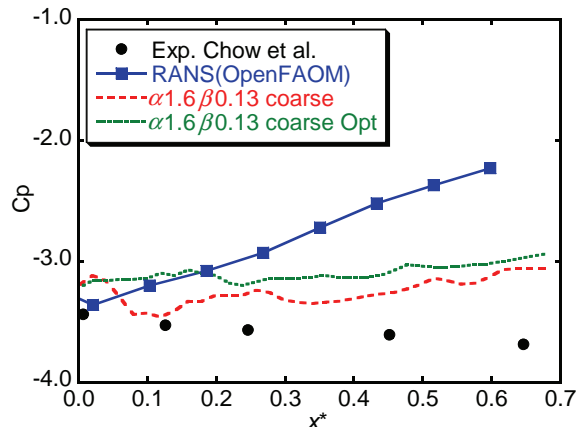
Figure 7. Pressure coefficient along vortex centerline with and without the optimization.

V. Wake evolution of the DLR-F6 wing-body model

A RANS flow field around the DLR-F6 wing-body model is employed to initialize the wake of a typical cruising aircraft. The RANS flow field is obtained by the DLR TAU-code with hybrid unstructured mesh where the number of mesh points is approximately 8.5 million.[33] The flow conditions of Mach number $M = 0.75$ and Reynolds number $\mathrm{Re} = 5.0 \times 10^6$ are considered. Note that the RANS flow field used here is not prepared for wake investigation but for the accurate prediction of aerodynamic forces such as lift and drag coefficients. Therefore, the mesh resolution in the wake is not enough to sharply capture wingtip vortices, which is a similar situation as in the previous NACA0012 wing case. Figure 8 shows the model geometry and contours of vorticity magnitude on several downstream planes.

For the normalization of quantities we use the following reference values assuming an elliptic load distribution,[1,4]

$$\Gamma_0 = \frac{2C_L U_\infty b}{\pi \Lambda}, \quad b_0 = \frac{\pi}{4} b, \quad w_0 = \frac{\Gamma_0}{2\pi b_0}, \quad t_0 = \frac{b_0}{w_0}, \tag{15}$$

where C_L, U_∞, b, and Λ represent a lift coefficient $C_L = 0.5$, uniform flow speed $U_\infty = 270$ m/s, wingspan $b = 1.172$ m, and wing aspect ratio $\Lambda = 9.5$, respectively. These values are from the experimental conditions.

American Institute of Aeronautics and Astronautics

Using these numbers the reference values for the normalization become $\Gamma_0 = 10.5 \text{ m}^2/\text{s}$, $b_0 = 0.92$ m, $w_0 = 1.8$ m/s, and $t_0 = 0.5$ s.
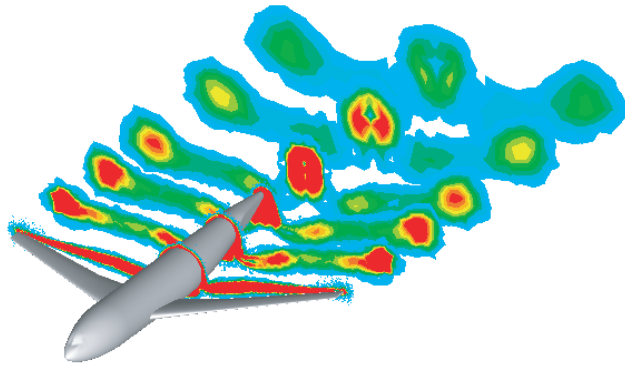

Figure 8. DLR-F6 model geometry and contours of vorticity magnitude on several downstream planes.

V.A.   Mesh resolution and switching wall-distance

Figure 9 shows the axial vorticity distribution on a plane at the distance of $x^* = 5.3$ from the trailing edge of the wingtip, which corresponds to $t^* = 0.03$ after the passage of the wingtip through the plane. The peak values of vorticity are also shown by the numbers. Here the mesh resolution and the switching wall-distance are varied. From a comparison among three different mesh resolutions shown in Figs. 9(a), (c), and (e), the finer mesh case clearly preserve vorticity distribution from the model's near field. Especially, the roll-up of a vorticity sheet from a main wing is clearly seen in Fig. 9(e). Peaks of vorticity are also large in the fine mesh case. The influence of the switching wall-distance is seen from Figs. 9(b), (c), and (d), where the result with $\beta = 0.06$ in Figs. 9(d) is close to the result of the fine mesh with the same switching wall-distance $\beta = 0.06$. It is same for the cases of Figs. 9(a) and (b).

The dependence of the results on the switching wall-distance is reduced by using the RANS flow field with mesh refinement in the wake region.[5] The other possibility to alleviate the dependency is to use the optimization of the switching wall-distance locally as shown in the previous NACA0012 case. The optimization of the switching wall-distance is effective to obtain a sharp wake while realizing smooth transition of RANS-LES flow fields in other regions. The optimization is not applied in the following results.

Figure 10 shows the circulation averaged between the nondimensional vortex core radii of 0.106 to 0.318, which corresponds to the circulation averaged between core radii of 5 to 15 m, denoted as Γ_{5-15}^*, used in real-scale field measurements.[34] In Fig. 10 the results from the RANS flow field is also shown. The horizontal axis shows the distance from the wingtip and the corresponding time is also shown on the top. The averaged circulations do not depend on the mesh resolution or the switching wall-distance, however, all cases appear to be larger than the RANS result.

Figure 11 shows the vortex core radius along downstream positions. The rapid growth of the core radius in the RANS case is due to the increase of mesh spacing away from the body surface. The vortex core radius after the switching is well represented by the mesh resolution and the switching wall-distance. The tendency is similar to the results in Fig. 9. And the growth rate in the LES is small compared to that of the RANS. For the finer mesh or smaller switching wall-distance case vortex core radius amounts to 2.5% of vortex spacing at $x^* = 5$, which corresponds to 2% of wingspan. The result coincides with field measurements.[35] On the other hand, the vortex core radius is 5.5% of the vortex spacing in the coarse mesh or the large switching wall-distance case.

The peak tangential velocity in Figure 12 shows similar tendency as the vortex core radius, i.e., finer mesh or smaller switching wall-distance realizes larger velocity value and vice versa. The peak tangential velocity in the RANS flow field is initially very large and quickly decreases. Figure 13(a) shows the wingtip of the DLR-F6 model and the tiny wingtip vortex in the RANS domain by axial vorticity. Figure 13(b) shows the tangential velocity profile close to wingtip. The peak value reaches to $V_\theta^* = 60$ and quickly decreases. It is also seen that the profile shows a two-scale profile in the beginning and evolves to a typical profile at around $x^* = 0.3$.
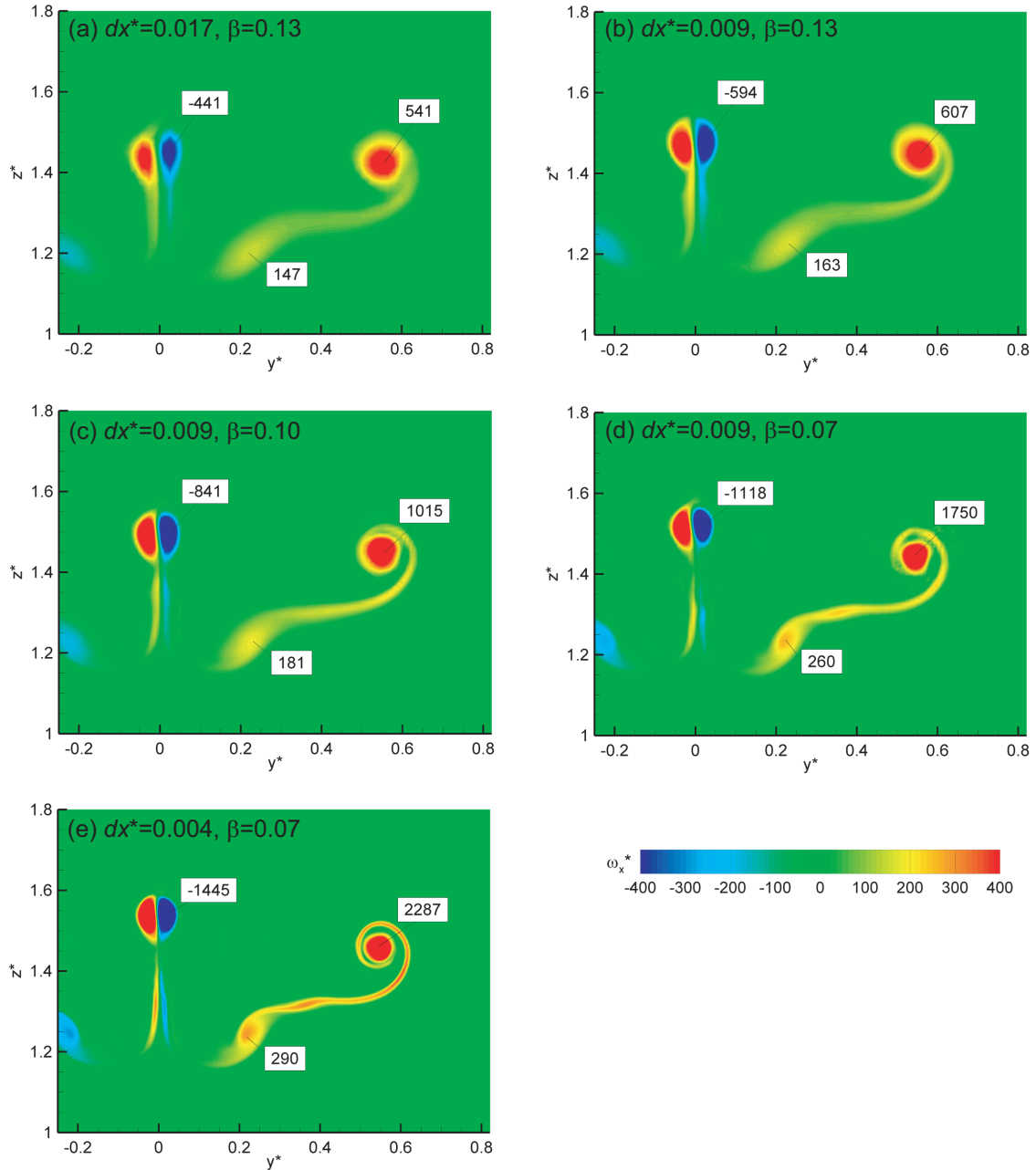
American Institute of Aeronautics and Astronautics

Figure 9. Axial vorticity distribution on a plane at the distance of $x^* = 5.3$ from the trailing edge of the wingtip for various mesh resolutions and switching wall-distances.
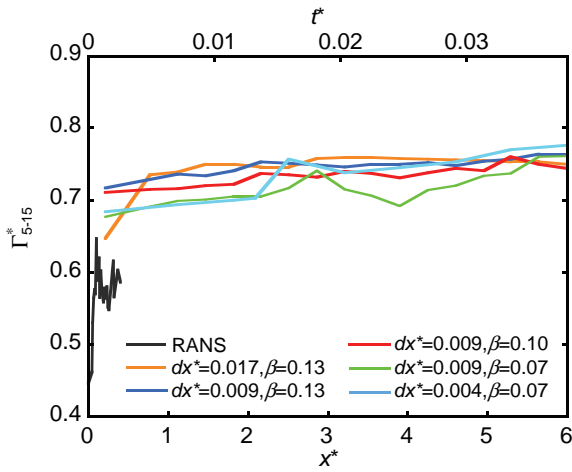
American Institute of Aeronautics and Astronautics

Figure 10. The averaged circulation in the near field for various mesh resolutions and switching wall-distances.

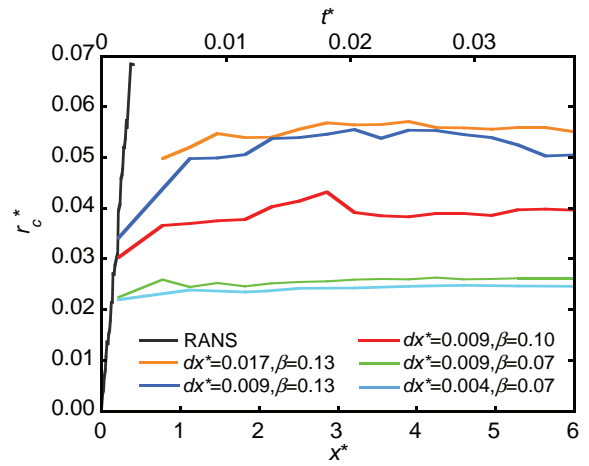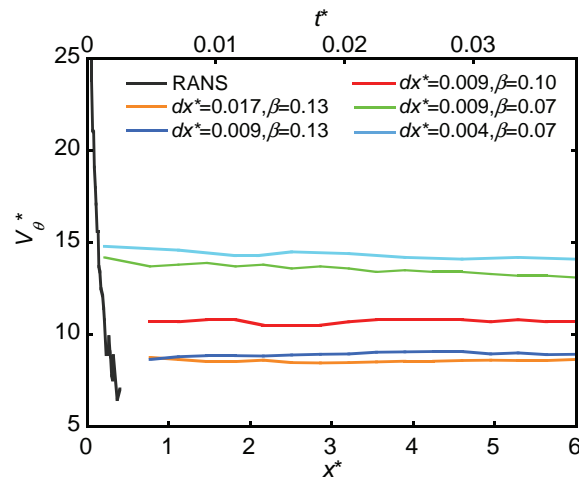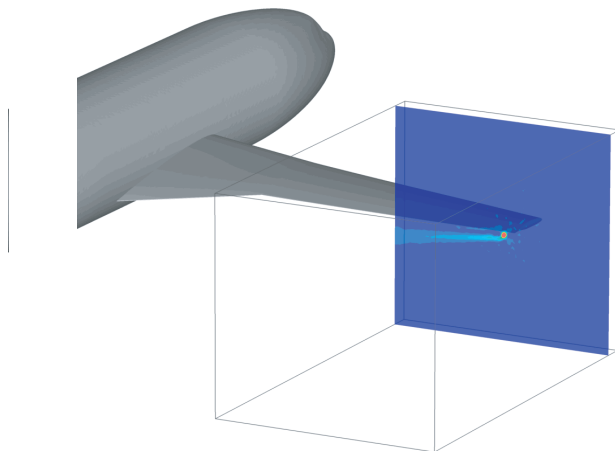**Figure 11.** Vortex core radius in the near field for various mesh resolutions and switching wall-distances.

Figure 12. Peak tangential velocity in the near field for various mesh resolutions and switching wall-distances.

(a) Wingtip and axial vorticity

(b) Tangential Velocity
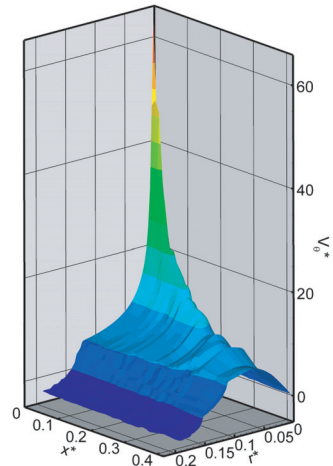
Figure 13. Wingtip and wingtip vortex in the RANS domain and the tangential velocity profile.

American Institute of Aeronautics and Astronautics

V.B.   Eddy viscosity initialization

Figure 14 shows the distribution of eddy viscosity on a plane at the distance of $x^* = 3.2$ from the trailing edge of the wingtip. As described above the eddy viscosity in the LES is increased by using a white noise so that the time-averaged LES eddy viscosity matches to the RANS eddy viscosity in the wake. The difference of the eddy viscosities mainly comes from the fuselage wake. In the coarser mesh resolution the produced eddy viscosity is similar as shown in Figs. 14(a) and (b). The effect of the added white noise is more clear in Figs. 14(c) and (d), where the fuselage wake is more disturbed by a white noise. In these cases, the eddy viscosity in the fuselage wake is increased while the distributions behind the main wing and the wingtip are not influenced.

The convergence history of the difference between the time-averaged LES eddy viscosity and RANS eddy viscosity is shown in Fig. 15. The difference decreases sufficiently and the gain which is also shown in Fig. 15 becomes constant after several tens time steps. In the present DLR-F6 case 1600 time steps are needed to initialize the wake, therefore, the convergence is sufficiently fast to use the eddy viscosity initialization during the wake initialization.
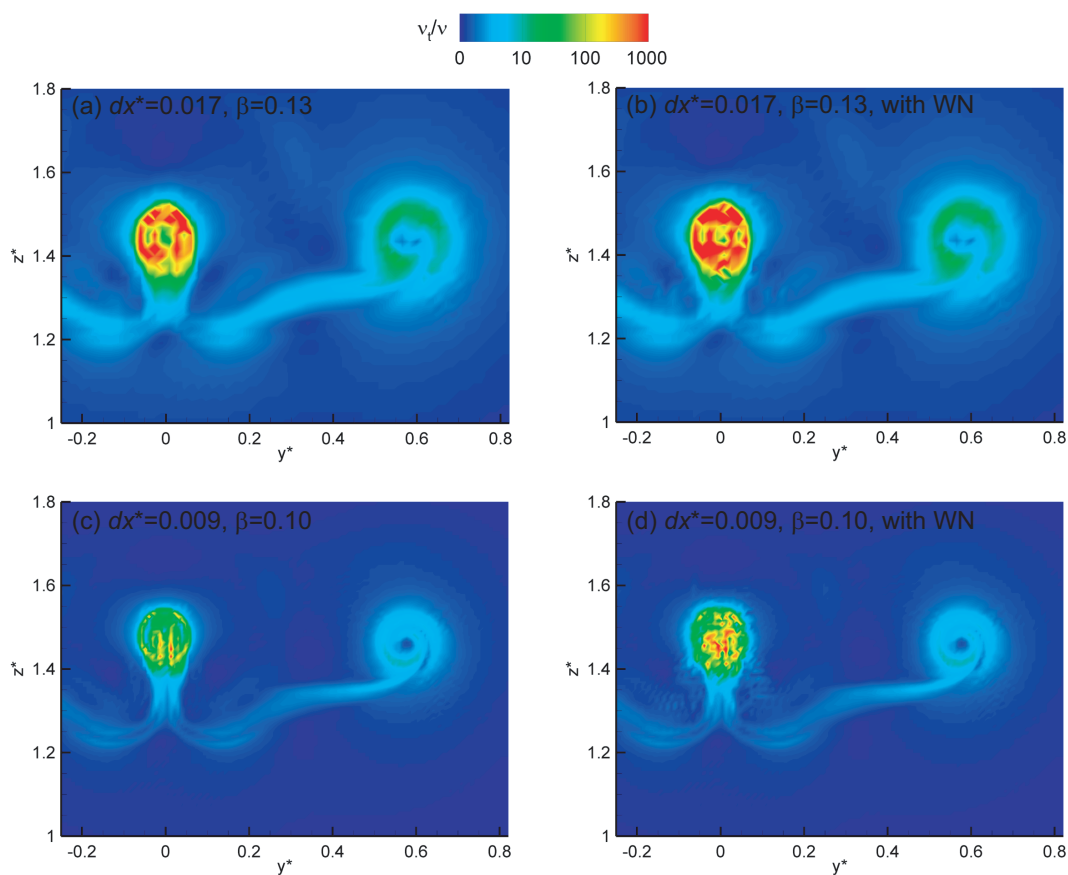

Figure 14. The distribution of eddy viscosity on a plane at the distance of $x^* = 3.2$ from the trailing edge of the wingtip for various mesh resolutions and switching wall-distances.
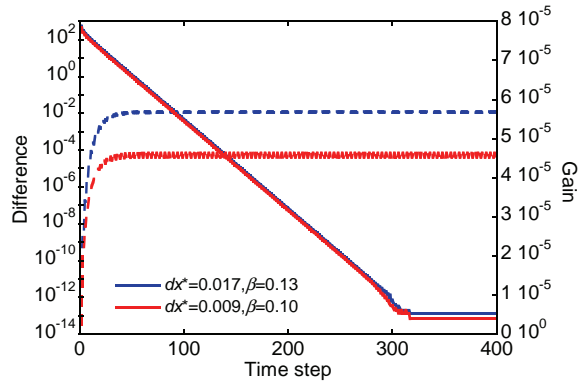
American Institute of Aeronautics and Astronautics

Figure 15. The history of the difference between the time-averaged LES eddy viscosity and RANS eddy viscosity as well as that of the gain for the PI control of a white noise.

V.C.   Wake roll-up and vortex evolution

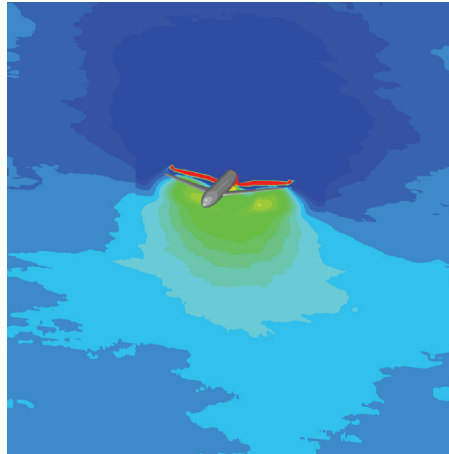Figure 16 shows a snapshot of the model advances through the turbulence environment where a velocity component in the flight direction is shown on the plane. To see the fluctuation of ambient turbulence, relatively low level of velocity magnitude is shown. The consideration of various ambient environment is straightforward in the present approach.

Figure 16. A snapshot of the model advances through turbulence environment where a velocity component in the flight direction is shown on the plane.

Figure 17 shows the wake roll-up and the subsequent evolution of a vortex pair. Here the ambient turbulence is characterized by eddy dissipation rate of $\varepsilon^* = 0.01$. Temperature stratification is not considered. The flow field is visualized by two levels of iso-vorticity surfaces (red: $|\omega^*| = 250$, blue transparent: $|\omega^*| = 65$). The midpoint the visualized wake in the flight direction corresponds to the representative position and the time labeled in each figure. Wingtip vortices and fuselage wake have large vorticity magnitude in the beginning. The jet-like fuselage wake decays relatively quickly while the wingtip vortices preserve large vorticity. The decayed fuselage wake and the vorticity from inboard wing (see also Fig. 9) wrap around the wingtip vortices adding disturbances around them. A stable vortex pair appears before Fig. 17(g). At $t^* = 8.8$, the vortex pair is highly disturbed and almost decayed.

Note that there is a difference of the vortex age between the both sides of the domain in the flight direction after the wake initialization. Here the flow field is inverted slicewise to close the domain periodically. The resulting LES domain is two times larger than the original one, i.e., two times larger computational cost, but it is possible to apply periodic boundary conditions also for the lateral boundaries. The inverted part of the domain in not shown in Fig. 17, however the influence of the boundary treatment is small.
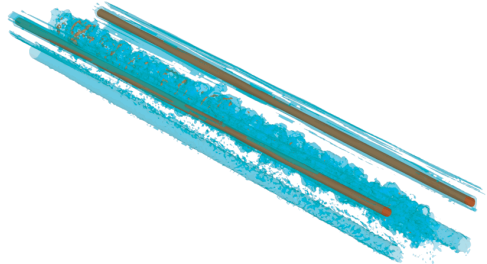
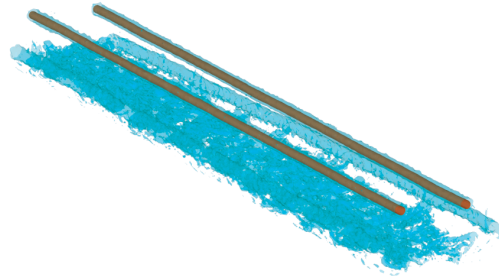American Institute of Aeronautics and Astronautics

(a) x^*=6.0 (t^*=0.04)
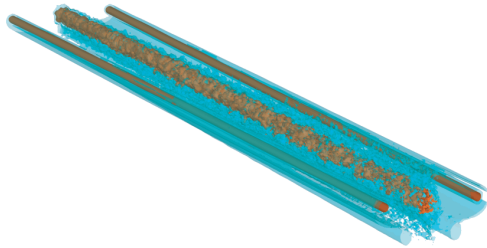
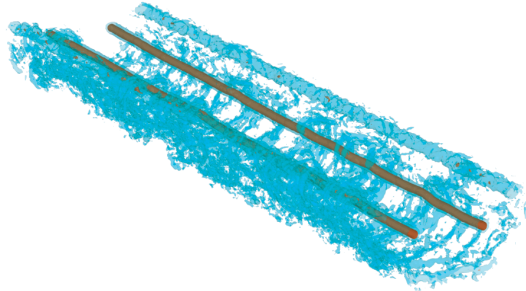(b) x^*=12.0 (t^*=0.08)

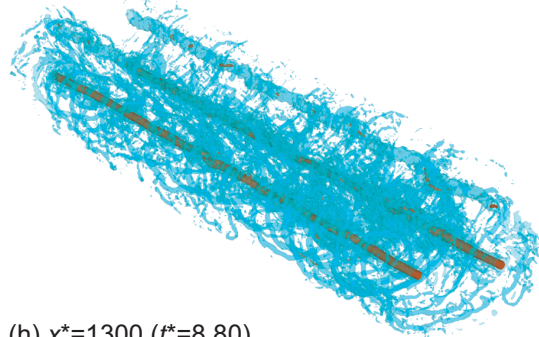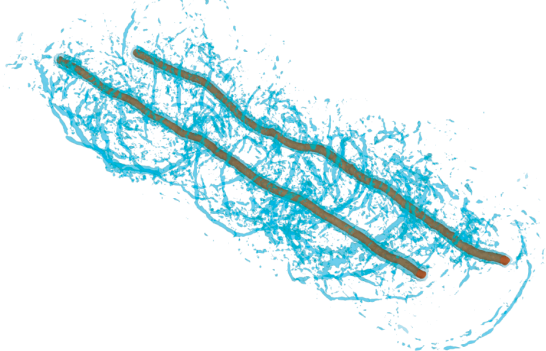(c) x^*=18.0 (t^*=0.12)

(d) x^*=47.0 (t^*=0.32)

(e) x^*=76.4 (t^*=0.52)

(f) x^*=117 (t^*=0.8)

(g) x^*=305 (t^*=2.07)

(h) x^*=1300 (t^*=8.80)

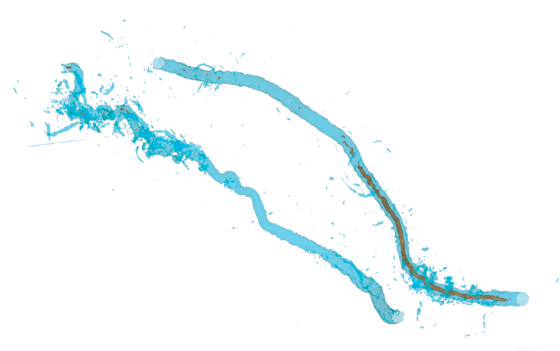**Figure 17. Time evolution of the iso-surfaces of vorticity magnitude (red: $|\omega^*| = 250$, blue transparent: $|\omega^*| = 65$).**

American Institute of Aeronautics and Astronautics

V.D. Vortex parameters

Figure 18 shows the time evolution of the averaged circulation with and without ambient turbulence ($\varepsilon^* = 0.01$). In this plot, Γ^*_{5-15} averaged along vortex centerlines in the domain and that evaluated on a cross-sectional plane are shown. The plots of Γ^*_{5-15} have a peak at around $x^* = 100$ ($t^* = 0.5$) and gradually decrease after this peak. The decrease of the Γ^*_{5-15} is slightly faster in the case without ambient turbulence. It is confirmed that the tendency is due to smaller vertical domain length in the case without ambient turbulence. Usually the ambient turbulence enhances the decrease of vortex circulation.

Figure 19 shows the time evolution of the vortex core radius. The cases shown here are the same as those of the Γ^*_{5-15}. The core growth rate until the end of the wake roll-up at $x^* = 200$ ($t^* = 1.3$) is small and it slightly increases after the roll-up. The averaged vortex core radius is smooth while that on a plane is fluctuated during the time evolution.

Figure 20 shows the time evolution of the vortex separation. The separation rapidly decreases at $x^* = 100$ ($t^* = 0.5$) when the averaged circulation reaches its peak value. The minimum value of vortex separation is 65% of b_0. After the roll-up the vortex separation approaches to b_0 in the clean case which agrees with that predicted for an elliptically loaded wing. In the weak turbulent case the separation keeps increasing after the roll-up. This might be one of the reason that the vortex linking is delayed.

Figure 21 shows the tangential velocity profiles at several distances. A broken line shows a fit using the Lamb-Oseen vortex model with $\Gamma^*_0 = 0.57$ and $r_c* = 0.05$. The decrease of peak tangential velocity and the increase of vortex core radius are confirmed.
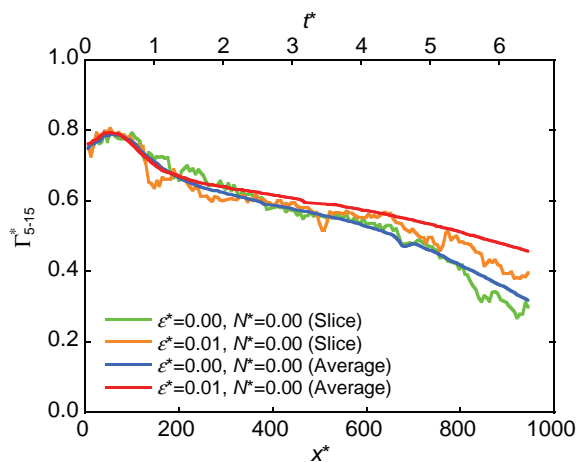

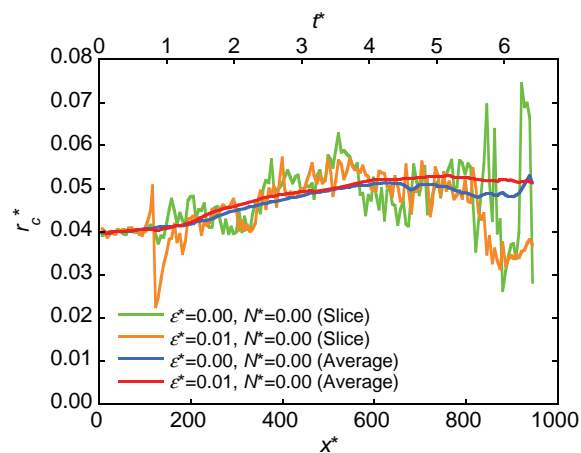Figure 18. Time evolution of the averaged circulation.

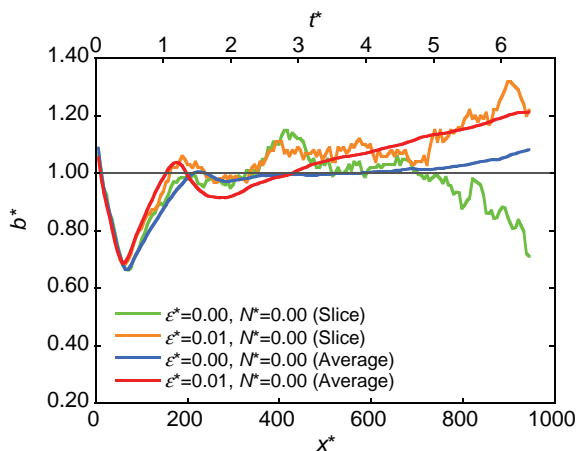Figure 19. Time evolution of the vortex core radius
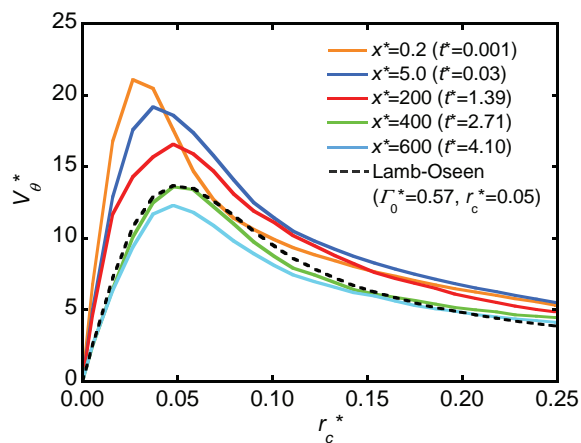

Figure 20. Time evolution of the vortex separation.

Figure 21. Tangential velocity profiles at several downstream distances.

American Institute of Aeronautics and Astronautics

VI.   Conclusions

LES of wake vortex evolution from its generation until vortex decay is performed by combining RANS and LES flow fields. The RANS flow field is employed in the LES as a forcing term sweeping through the ground-fixed LES domain. The eddy viscosity initialization to match the time-averaged LES and RANS eddy viscosities as well as the optimization of the switching wall-distance are proposed.

The methodology is tested using the NACA0012 wing. The present approach achieves comparable results with the experiment by using the RANS flow field which is not accurate enough to reproduce experimental results in the downstream. The present approach only uses the very near field of the RANS flow field and then the solution process switches to the LES. This way the wing-tip vortex properties observed in the experiment are reproduced well.

Further, the roll-up process of the wake initialized by the DLR-F6 model is simulated. The roll-up processes of the vorticity sheet emanating from the wing and tight vortices from the wingtip are simulated. A stable vortex pair appears after this. The growth of vortex core radius is small especially after the roll-up, where the vortex core radius still depends on the mesh resolution considered here.

Acknowledgments

References

[1]Gerz, T., Holzäpfel, F., and Darracq, D., "Commercial Aircraft Wake Vortices," *Progress in Aerospace Science*, Vol. 38, No. 3, 2002, pp. 181–208.

[2]Minnis, P., Young, D. F., Ngyuen, L., Garber, D. P., Jr., W. L. S., and Palikonda, R., "Transformation of Contrails into Cirrus during SUCCESS," *Geophysical Research Letters*, Vol. 25, No. 8, 1998, pp. 1157–1160.

[3]Schumann, U., Graf, K., and Mannstein, H., "Potential to Reduce the Climate Impact of Aviation by Flight Level Change," AIAA Paper 2011–3376, 2011.

[4]Breitsamter, C., "Wake Vortex Characteristics of Transport Aircraft," *Progress in Aerospace Science*, Vol. 47, No. 2, 2011, pp. 89–134.

[5]Stumpf, E., "Study of Four-Vortex Aircraft Wakes and Layout of Corresponding Aircraft Configurations," *Journal of Aircraft*, Vol. 42, No. 3, 2005, pp. 722–730.

[6]Rossow, V. J., "Lift-Generated Vortex Wakes of Subsonic Transport Aircraft," *Progress in Aerospace Science*, Vol. 35, No. 6, 1999, pp. 507–660.

[7]Leweke, T. and Williamson, C. H. K., "Cooperative Elliptic Instability of a Vortex Pair," *Journal of Fluid Mechanics*, Vol. 360, 1998, pp. 85–119.

[8]Nomura, K. K., Tsutsui, H., Mahoney, D., and Rottman, J. W., "Short-Wavelength Instability and Decay of a Vortex Pair in a Stratified Fluid," *Journal of Fluid Mechanics*, Vol. 553, 2006, pp. 283–322.

[9]Laporte, F. and Corjon, A., "Direct Numerical Simulation of the Elliptic Instability of a Vortex Pair," *Physics of Fluids*, Vol. 12, No. 5, 2000, pp. 1016–1031.

[10]Han, J., Lin, Y., Schowalter, D. G., and Pal Arya, S., "Large Eddy Simulation of Aircraft Wake Vortices Within Homogeneous Turbulence: Crow Instability," *AIAA Journal*, Vol. 38, No. 2, 2000, pp. 292–300.

[11]Proctor, F. H., Hamilton, D. W., and Han, J., "Wake Vortex Transport and Decay in Ground Effect: Vortex Linking with the Ground," AIAA Paper 2000–0757, 2000.

[12]Holzäpfel, F., Gerz, T., Frech, M., and Dörnbrack, A., "Wake Vortices in Convective Boundary Layer and Their Influence on Following Aircraft," *Journal of Aircraft*, Vol. 37, No. 6, 2000, pp. 1001–1007.

[13]Holzäpfel, F., Gerz, T., and Baumann, R., "The Turbulent Decay of Trailing Vortex Pairs in Stably Stratified Environments," *Aerospace Science and Technology*, Vol. 5, No. 2, 2001, pp. 95–108.

[14]Holzäpfel, F., Misaka, T., and Hennemann, I., "Wake-Vortex Topology, Circulation, and Turbulent Exchange Processes," AIAA Paper 2010–7992, 2010.

[15]Unterstrasser, S. and Gierens, K., "Numerical simulations of contrail-to-cirrus transition - Part 1: An extensive parametric study," *Atmospheric Chemistry and Physics*, Vol. 10, 2010, pp. 2017–2036.

[16]Paugam, R., Paoli, R., and Cariolle, D., "Influence of Vortex Dynamics and Atmospheric Turbulence on the Early Evolution of a Contrail," *Atmospheric Chemistry and Physics*, Vol. 10, 2010, pp. 3922–3952.

[17]Misaka, T., Holzäpfel, F., Gerz, T., Manhart, M., and Schwertfirm, F., "Large-Eddy Simulation of Wake Vortex Evolution from Roll-Up to Vortex Deacy," AIAA Paper 2011–1003, 2011.

[18]Manhart, M., "A Zonal Grid Algorithm for DNS of Turbulent Boundary Layer," *Computer & Fluids*, Vol. 33, No. 3, 2004, pp. 435–461.

[19]Kobayashi, M. H., "On a Class of Páde Finite Volume Methods," *Journal of Computational Physics*, Vol. 156, No. 1, 1999, pp. 137–180.

[20]Hokpunna, A. and Manhart, M., "Compact Fourth-order Finite Volume Method for Numerical Solutions of Navier-Stokes Equations on Staggered Grids," *Journal of Computational Physics*, Vol. 229, No. 20, 2010, pp. 7545–7570.

[21]Hokpunna, A., "Compact Fourth-order Scheme for Numerical Simulations of Navier-Stokes Equations," *Ph.D Thesis, Technische Universität München, Germany (2009)*.

[22]Hirt, C. W. and Cook, J. L., "Calculating Three-dimensional Flows Around Structures and Over Rough Terrain," *Journal of Computational Physics*, Vol. 10, No. 2, 1972, pp. 324–340.

[23]Brandt, A., Dendy Jr., J. E., and Ruppel, H., "The Multigrid Method for Semi-Implicit Hydrodynamics Codes," *Journal of Computational Physics*, Vol. 34, No. 3, 1980, pp. 348–370.

[24]Williamson, J. H., "Low-storage Runge-Kutta Schemes," *Journal of Computational Physics*, Vol. 35, No. 48, 1980, pp. 48–56.

[25]Meneveau, C., Lund, T. S., and Cabot, W. H., "A Lagrangian Dynamic Subgrid-scale Model of Turbulence," *Journal of Fluid Mechanics*, Vol. 319, 1996, pp. 353–385.

[26]Coton, P., "Study of Environment Effects by Means of Scale Model Flight Test in a Laboratory," 21st ICAS Congress, 13–18 September 1998, Melbourne, ICAS–98–391, 1998.

[27]Fujii, K., "Unified Zonal Method Based on the Fortified Solution Algorithm," *Journal of Computational Physics*, Vol. 118, No. 1, 1995, pp. 92–108.

[28]Kalnay, E., *Atmospheric Modeling, Data Assimilation and Predictability*, Cambridge University Press, 2003.

[29]Czech, M. J., Miller, G. D., Crouch, J. D., and Strelets, M., "Near-field Evolution of Trailing Vortices Behind Aircraft with Flaps Deployed," AIAA Paper 2004–2149, 2004.

[30]Chow, J., Zilliac, G., and Bradshow, P., "Turbulence Measurements in the Near Field of a Wingtip Vortex," NASA TM–110418, 1997.

[31]Dacles-Mariani, J., Zilliac, G., Chow, J., and Bradshow, P., "Numerical/Experimental Study of a Wingtip Vortex in the Nearfield," *AIAA Journal*, Vol. 33, No. 9, 1995, pp. 1561–1568.

[32]http://www.openfoam.com/.

[33]Brodersen, O., Eisfeld, B., Raddatz, J., and Frohnapfel, P., "DLR Results from the Third AIAA Computational Fluid Dynamics Drag Prediction Workshop," *Journal of Aircraft*, Vol. 45, No. 3, 2008, pp. 823–836.

[34]Holzäpfel, F., Gerz, T., Köpp, F., Stumpf, E., Harris, M., Young, R. I., and Dolfi-Bouteyre, A., "Strategies for Circulation Evaluation of Aircraft Wake Vortices Measured by Lidar," *Journal of Atmospheric and Oceanic Technology*, Vol. 20, No. 8, 2003, pp. 1183–1195.

[35]Delisi, D. P., Greene, G. C., Robins, R. E., Vicroy, D. C., and Wang, F. Y., "Aircraft Wake Vortex Core Size Measurements," AIAA Paper 2003–3811, 2003.